

Research Article

FEM Design of a Cutting-Edge Support System for Micro-GT

Fabrizio Stefani , Ramon Francesconi, and Andrea Perrone

Department of Mechanical, Energy, Management, and Transportation Engineering, University of Genova, Via all'Opera Pia 15, 16145 Genova, Italy

Correspondence should be addressed to Fabrizio Stefani; stefani@unige.it

Received 3 January 2018; Accepted 7 February 2018; Published 15 March 2018

Academic Editor: Huseyin Çimenoglu

Copyright © 2018 Fabrizio Stefani et al. This is an open access article distributed under the Creative Commons Attribution License, which permits unrestricted use, distribution, and reproduction in any medium, provided the original work is properly cited.

The design of the support system (shaft, bearings, and mechanical coupling devices) of the rotor plays a key role in the development of efficient micro-gas turbines (micro-GTs) for distributed power generation. Foil air bearings are the most widespread technical solution well suited to design a reliable support system, although they cannot withstand a large number of start-stop cycles of the units. In order to overcome such limitation, we have recently proposed an innovative support system that takes advantage of spline couplings and two bearing types (e.g., air and rolling-element bearings). The devised support system employs splines as both convenient coupling systems and actuators for the load partition between the two bearing types. In the present work, the helical spline coupling is studied by means of structural FEM analyses including contact simulation in order to design the support system. Numerical results confirm previous findings in that the load transfer through the spline coupling is mainly a function of the helix angle. In addition, friction factor and structural stiffness cannot be neglected in the accurate design of the spline coupling. Such design parameters are now included in the proposed design procedure, which formerly assumed frictionless contact and rigid bodies.

1. Introduction

Due to the high speeds of rotation (in the order of 10^5 rpm) and operating temperatures (up to 1000°C), bearings are among the most stressed mechanical components in micro-gas turbine (micro-GT) systems, and therefore lubrication as well as a support system plays a key role in the operation of the machine.

The adoption of a single type of bearing is typical of bearing arrangements that are usually employed in commercial micro-GT units. Existing micro-GT installations employ foil (aerodynamic) and rolling-element bearings, where the former solution is certainly more innovative and promising. Conventional bearings (rolling-element type) are still used in micro-GT systems for reasons of size and cost; for example, since 1999, Capstone have offered a version of their Model 330 microturbine with a ball-bearing-based compressor and continued to offer the ball bearing compressor as an economical option for medium-pressure applications. Differently, oil-free support systems rely on the main patent of Capstone technology, which has been developed by the US National Aeronautics and Space Administration (NASA).

However, in the design of a novel support system for the shaft, it is reasonable to consider magnetic bearings as a convenient alternative. Indeed, their advantages over conventional bearings are as follows: oil-free operation, extreme temperature as well as active control for active magnetic bearings (AMBs) [1], ease of miniaturization [2], and independence of external energy input for passive magnetic bearings (PMBs) [3]. Usually, the advantage of the resistance to high temperatures makes AMBs the preferred choice for the application at hand.

Despite such features of magnetic supports, foil air bearings are considered the first choice for oil-free micro-GT applications. Indeed, in comparison with AMBs, foil bearings have lower upfront cost and fewer failure modes [4] and do not consume energy to supply electromagnets. However, magnetic bearings ensure longer life, lower friction, and potentially less severe failures.

Therefore, magnetic bearings are preferred for large engines operating at high loads and relatively lower speed, while the opposite is true for foil bearings. Indeed, air bearings do not carry high loads at lower speeds, as gas viscosity is low, and adhesion of their tribological coatings to

large diameter shafts under large centrifugal forces is difficult [1].

With regard to conventional bearings (rolling-element type), often used in low-power micro-GT units for reasons of size and cost, the fundamental problem is the duration that is limited by the phenomenon of fatigue and is load-dependent. Indeed, for these supports, the “carrying capacity” is the ability of the bearing to carry a given load for a predetermined number of cycles or revolutions [5].

On the other hand, foil bearings have a life dependent on the number of starts and stops of the machine. Rubbing between the top foil and journal surfaces, which are preloaded against each other, occurs at a low speed when the shaft is not airborne. Therefore, starts and stops are the only events in which the bearing sheets are prone to wear. Hence, expensive tribological coatings on both the top foil and the shaft are required [6, 7]. The start/stop performance is important as micro-GT units are expected to withstand the wear of daily starts and stops. A US government/industry program has got recently underway, where the machines are tested to assess their performance including start and stop capabilities.

The proof of the research effort to improve the start/stop performance of air bearing yields is given by many published works. For example, solid lubrication has been studied in many pertinent papers [6, 8–10]. Advances in such field are turned into new patents. For example, a powder having lubricating properties can be interposed between the bearing surfaces in order to provide lubrication of foil bearings at low speed, when the journal is not airborne [11]. It forms a film whose lubricity and adhesion properties are capable of reducing torque and increasing bearing life. The powder acts during mixed lubrication and it is displaced when the journal is airborne. Nevertheless, it may influence aerodynamic lubrication to a certain extent. In any case, solid lubrication cannot get rid of wear completely.

In [12], we have presented the conceptual design of a new support system that is capable of removing axial load from the air thrust bearing during mixed lubrication regime, thus eliminating start/stop wear. The axial load is shared by two axial bearings of different types. Indeed, the invention is based on the idea that since each bearing type has different strengths and weaknesses, using different types of bearings in the same support system yields benefits. Accordingly, the proposed innovation overcomes the above-cited flaws of the support systems adopted in micro-GT and, at the same time, takes advantage of the best qualities of different bearing types. Indeed, it is capable of matching different types of bearings and managing the relevant loads by means of suitable shaft-hub couplings.

A convenient solution for the coupling between the shaft and hubs of compressor and turbine rotors may be the use of splines. Indeed, aircraft engines adopt splines and many gas turbines are derivatives of aircraft engines [13]. In comparison with shrink fits, such design solution, without heavily limiting the transmissible torque as in the case of keys, boasts the considerable advantage of ease in assembly and disassembly [14]. This may be particularly interesting for a small machine like a microturbine, in order to facilitate maintenance and inspections. In addition, in comparison with keys, spline

couplings provide higher load carrying capacity that often turns into better durability and allows for a certain amount of angular misalignment as well as relative sliding between the shaft and the hub [15].

In this work, the use of a helical spline as an actuator capable of transferring axial load between two bearings of convenient type is studied. The operation of helical splines is analyzed by means of a nonlinear structural model of the hub-shaft assembly and the finite element method (FEM).

2. Case Study

Table 1 reports the main data of a 100 kW micro-GT unit designed in previous works [12, 16]. It also includes the relevant loads, that is, the turbine and compressor thrusts T_t and T_c , respectively, as well as the vertical load W . Such thrusts, whose positive direction is from the compressor to the turbine, are the result of the axial forces exerted on the blades and on the backside of the impellers by the working fluid. Differently, load W is due to the weight of the rotor. Two load cases (referred to as A and B) characterized by the same modulus (a reference value of 500 N) of the resultant thrust,

$$T_{\text{ref}} = T_r + T_c, \quad (1)$$

are studied. Particularly, in case A, both the turbine and the compressor impeller thrusts are directed toward the external side of the unit ($T_t > 0$, $T_c < 0$). Differently, in case B, both thrusts are directed toward the inner side of the machine and the total thrust direction reverses too ($T_t < 0$, $T_c > 0$). As detailed in [12], for different impeller geometries, which may yield different pressures on the clearances between the casing cover and impeller back shroud (backside pressures), the impeller thrusts can be either external or internal, as in cases A and B, respectively.

Compressor and turbine axial loads are the most significant in a microturbine, since they are 10x greater than the radial ones (shaft weight). For the application in this study, due to high axial loads, durations of rolling-element bearings correlated to fatigue phenomenon are very low compared with the life of a micro-GT unit (60.000–80.000 hours) [12].

3. The Innovative Layout

As already explained in detail in [12], the main goal of the novel assembly is to separate the axial load exerted by the impellers into two parts. The first part of the thrust directly loads the main axial bearing, without getting through the shaft. This type of load application will be referred to as “direct” in the following. Differently, the second part is managed like in conventional support systems; that is, the impellers exert the thrust on the shaft that, in turn, transfers it to an additional (auxiliary) axial bearing.

Particularly, for the sake of simplicity, only the axial load exerted by the turbine impeller is separated, as it is higher than the compressor one. The direct application of the axial load is not a new idea, as reported in [17]. Differently, in such reference patent, the compressor impeller in place of the turbine one directly exerts thrust on the axial bearing.

TABLE 1: Design data of the reference micro-GT unit as well as the spline coupling.

	Design variable [unit]	Value
Micro-GT data	Rotational speed N [rpm]	70,000
	Shaft diameter D_s [mm]	15
	Power P [kW]	110
	Pressure ratio	4
	Turbine thrust T_t [N]	1100 (case A), -1700 (case B)
	Compressor thrust T_c [N]	-600 (case A), 1200 (case B)
	Total axial load T_{ref} [N]	500 (case A), -500 (case B)
	Radial load (rotor weight) W [N]	40
	Turbine torque M_t [N m]	30
	Compressor torque M_c [N m]	-15
Helical spline coupling data	Type	ISO 141982 (E), shaft and hub $6 \times 11 \times 14$
	Length L [mm]	220
	Outer diameter D_o [mm]	220
	Spline inner (or pitch) radius r_p [mm]	5.5
	Spline outer radius r_o [mm]	7
	Number of splines n	6
	Side distance B [mm]	3
	Young's modulus [GPa]	206
	Poisson's ratio	0.3

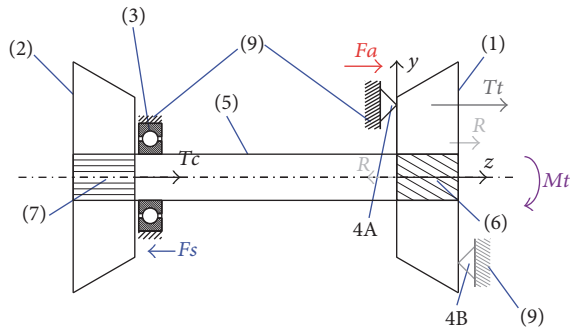


FIGURE 1: Static scheme (axial forces) of the innovative rotor operating in nominal conditions.

In order to take advantage of the above-cited peculiar attitudes of each bearing type, main and auxiliary bearings are different (e.g., the main thrust support is a foil air bearing, while the auxiliary one is rolling-element type).

Therefore, such thrust load separation allows the support system to switch between the two types of bearings automatically when the unit ends the transient operation. In addition, it employs helical splines as both convenient shaft-impeller coupling systems and actuators suitable to adjust the entity of the load transferred to each thrust bearing. Indeed, a convenient partitioning of the turbine thrust is required in order to optimize the behavior of the support system [12].

Figure 1 depicts all of the axial forces acting on the rotor components in nominal conditions, according to the modifications resulting from the innovation. F_a is the axial force

that the main axial bearing (4) exerts on the turbine impeller (1), while F_s is the thrust that the auxiliary axial bearing (3) exerts on the shaft (5). Considering force equilibrium in static condition yields

$$\begin{aligned} F_a &= -T_t - R \\ F_s &= T_c - R. \end{aligned} \quad (2)$$

Constraints (4A) and (4B) in Figure 1 simulate in case either A or B, respectively, the main axial bearing (4) that carries the load F_a . The axial forces R are the (equal) action and reaction that the turbine impeller exerts on the shaft through the helical spline and will be referred to as load transfer. Its modulus is lower than the ones of turbine and compressor thrust. The total thrust that acts on the shaft is F_s and is carried by the auxiliary axial bearing (3). The torque M_t is the resisting torque of the turbine due to the pressure exerted on the relevant blades.

In the case of positive resultant thrust (case B, $T_t < 0$), equation (2) yields that the constraint modeling the main thrust bearing in Figure 1 must be (4B); that is, the axial force exerted by the bearing on the impeller is positive ($F_a > 0$). Contrarily, in case A, since $F_a < 0$, the constraint must be (4A). In other words, the location of the thrust main bearing (4) with reference to the machine frame should be different in cases A and B.

For example, the runner of the main thrust bearing (4) might be mounted on the high-pressure side of the impeller (1) and on its opposite side in cases B and A, respectively. The location of the pads of bearing (4) might be modified accordingly. Nevertheless, such solution including single

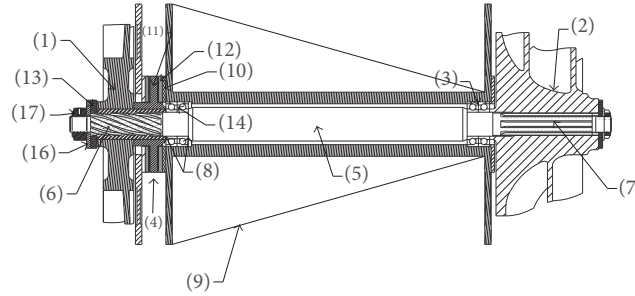


FIGURE 2: Section of the micro-GT support system assembly designed according to the invention.

TABLE 2: Components and details numbered in the assembly figures.

(1)	Turbine (impeller)
(2)	Compressor (impeller)
(3)	Journal bearing/auxiliary thrust bearing
(4)	Main thrust bearing
(5)	Shaft
(6)	Helical spline coupling
(7)	Spline
(8)	Shaft shoulder
(9)	Frame
(10)	Pad spacer
(11)	Thrust runner
(12)	Thrust pads
(13)	Turbine impeller spacer
(14)	Journal bearing
(15)	Inner ring shoulder of journal bearing
(16)	Flat washer
(17)	Locking ring nut

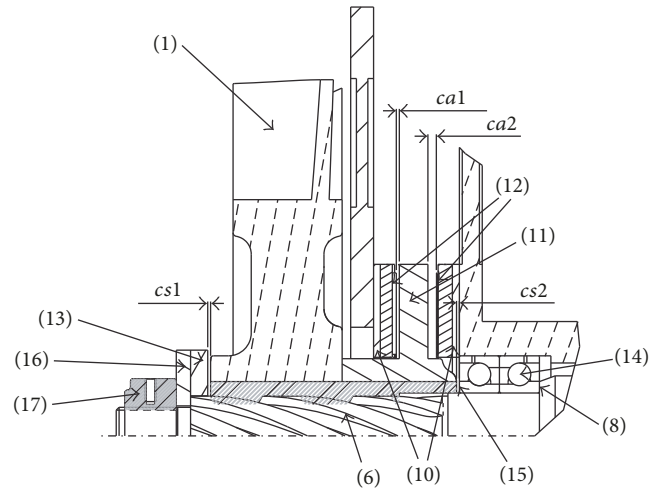


FIGURE 3: Clearances between the components of the support system.

effect thrust bearings would not be optimal from the point of view of the machine layout.

A more straightforward solution consists in manufacturing a thrust collar/runner that is either an integral part of the turbine impeller or rigidly fastened to it, so that pads of bearing (4) can be located on both sides of the runner regardless of the thrust direction. Accordingly, the assembly drawing of the invention is reported in Figure 2. Such support system is suited to both positive and negative nominal thrusts (with a consistent choice of the helix angle of the spline coupling) as well as transient loading conditions. The numbered components are listed in Table 2. In this case, the main thrust bearing (4) is a double-effect foil air bearing instead of a single effect one. In other words, the pads (12) are located on both sides of the thrust collar/runner (11). The group of pads on the side that carries the thrust load in nominal working conditions is termed the “loaded” or active bearing, while the other group, on the opposite side of the thrust collar, is called the “slack” side or inactive bearing.

In Figures 2 and 3, a second set of (nonlocating) angular contact bearings (14) in back-to-back arrangement, which

is not included in the scheme of Figure 1, is added to the assembly near the turbine. In this case, at low speeds, the annular shoulder (8) does not receive the thrust load directly from the turbine impeller (1). Indeed, it exerts the thrust on the inner ring side (15) (Figure 3) of the bearing (14). Anyway, the behavior of the invention does not change, as the bearing (14) is not constrained in the axial direction and, therefore, no axial load is transferred to the frame (9).

The flat washer (16) is fastened to the shaft (5) with a locking ring nut (17). The spacer (13) is mounted between the washer (16) and the impeller (1) in order to adjust the axial gap of the turbine hub-shaft coupling. Similarly, two spacers (10) are employed to adjust the axial clearance of the air bearings (the active as well as the inactive one).

Particularly, as shown in Figure 3, the total axial clearance c_{st} of the turbine hub-shaft coupling is the sum of the clearances c_{s1} and c_{s2} ($c_{st} = c_{s1} + c_{s2}$). In the following, the gap between pads and the runner of the air bearings is the desired operating clearance and it is referred to as “hot” clearance. The gap c_{s1} is the clearance between the spacer (13) and the turbine impeller (1), while c_{s2} is the gap between the turbine impeller (1) and the inner ring side (15) of the bearing (14). Similarly, the total hot clearance c_{at} of the double-effect air bearing (4) is given by the sum of two contributions c_{a1} and

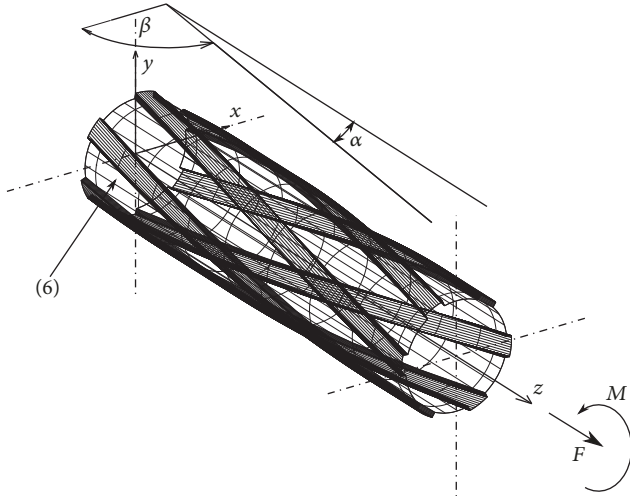


FIGURE 4: Helix angles and reference system of spline coupling.

c_{a2} , which are the hot clearances between runner (11) and pads (12) of the active and the inactive bearing ($c_{at} = c_{a1} + c_{a2}$).

In order to avoid wear of the double-effect air bearing (4) due to dry contact between the runner and pads at low speed, its total hot clearance c_{at} must be higher than the clearance of the turbine hub-shaft coupling c_{st} ($c_{at} > c_{st}$). Indeed, the axial clearance c_{st} of the coupling (6) must be very little (in the micron-length scale). Anyway, c_{st} must be greater than the equivalent RMS roughness of the two contact surfaces at the impeller (1)/inner ring side (15) interface (or impeller/annular shoulder (8), if the bearing (14) is not employed), in order to provide the relief of the secondary axial bearing (3) over the speed at which the runner (11) becomes airborne.

4. FEM Analysis of the Spline Coupling

The law of load distribution followed during nominal operation by the helical spline pair, employed as a mechanical actuator besides a simple coupling system, must be determined. To this end, a campaign of FEM structural analyses has been carried out on a model of a helical spline coupling with parallel-side profiles by varying the design lead angle β from 45 to 135 deg (admissible range for helical gears). Design data of the spline coupling are reported in Table 1. The reference system, the lead angle β , and the helix angle α (geometric complement of β) of the spline coupling model are shown in Figures 1 and 4. In agreement with the lead angle definition, the middle of the range ($\beta = 90$ deg) corresponds to a spline with rectilinear generatrices (straight teeth).

The virtual model, fully developed by means of the ANSYS Parametric Design Language (APDL) in ANSYS 15.0, is parametric in that the geometry is completely defined by parameters (diameters, axial length, number of keys, and helix angle). The three-dimensional models of hub and shaft are meshed by means of first-order isoparametric structural solid elements (SOLID185), as shown in Figures 5(a) and 5(b), respectively (for $\beta = 135$ deg). Then, the two meshed

components are matched and their interface is modeled by means of surface-to-surface contact elements (CONTA173 and TARGE170) with zero initial gap and isotropic friction (friction factor $f = 0, 0.15, 0.3, \text{ and } 0.45$). The resulting nonlinear model of the coupling includes 103,566 nodes and 104,160 elements. The default augmented Lagrangian solver is employed. The elapsed time required to calculate results for all the considered ranges of β with a step of 5 deg (a single curve in the plots discussed below) is roughly 4-5 hours on a conventional PC (AMD FX-8350 eight-core processor, 4 GHz clock, 16 GB RAM). Although a second-order mesh (including SOLID186, CONTA174 element types) has been also tested, due to the much higher elapsed time, the relevant results have been only used in order to confirm the results obtained by means of the first-order mesh. Some second-order calculations have confirmed the trends published in the following. A cyclic model has also been tested in order to reduce the elapsed computational time. Nevertheless, it does not give consistent results under torque load and when the lead angle is small.

Initially, case B (the case with higher thrust) is simulated after it is subdivided into two simpler load cases; that is, the hub is loaded either by an axial force F or by a torque M (Figure 4). Particularly, as suggested by Figure 1 the nominal thrust $F = T_t$ and torque $M = M_t$ (Table 1) are applied to one side of the hub. Therefore, in the former load case, the hub is loaded by a compressive stress ($F < 0$), while in the latter the torque acts on the hub so that, due to the threaded connection, it tends to move with reference to the shaft either in the positive z direction if $\beta < 90$ deg or in the negative one if $\beta > 90$ deg. Since reversing the direction of the torque load yields periodic results (with period $\beta = 90$ deg) and the hub stress due to the thrust load relevant to case B is compressive between the blades and the bearing, unidirectional loads are considered. Finally, a combined load case is simulated, where force and torque are simultaneously applied.

The axial load on the hub side is obtained by distributing a suitable uniform pressure on the corresponding surface, in which the axial section localized at $z = L$ is shown in Figure 6(a). Differently, the torque is generated on the same section ($z = L$) either by means of a multipoint constraint (MPC) contact region that is bonded to a pilot node transmitting the torque or, equivalently, by applying circumferential nodal forces proportional to the radial coordinate (Figure 6(b)). At the opposite side of the assembly (section localized at $z = 0$), the nodes lying on the shaft are fully constrained, while those on the hub section cannot move in the axial direction, as summarized by Figure 6(c).

5. Results and Discussion

Figures 7 and 8 plot the partition of axial load between the hub and the shaft as a function of the lead angle for axial force and torque load cases, respectively. In these figures, if not differently specified by means of a suitable friction factor label, FEM results are obtained by means of frictionless contact elements. The plotted FEM model axial reactions R_h and R_s of the hub and the shaft, respectively, are computed by

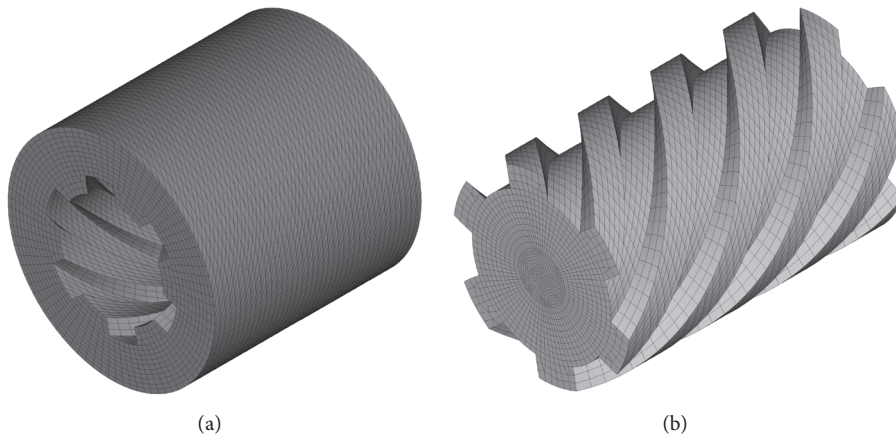


FIGURE 5: Finite element mesh of the helical spline coupling ($\beta = 135$ deg): (a) hub, (b) shaft.

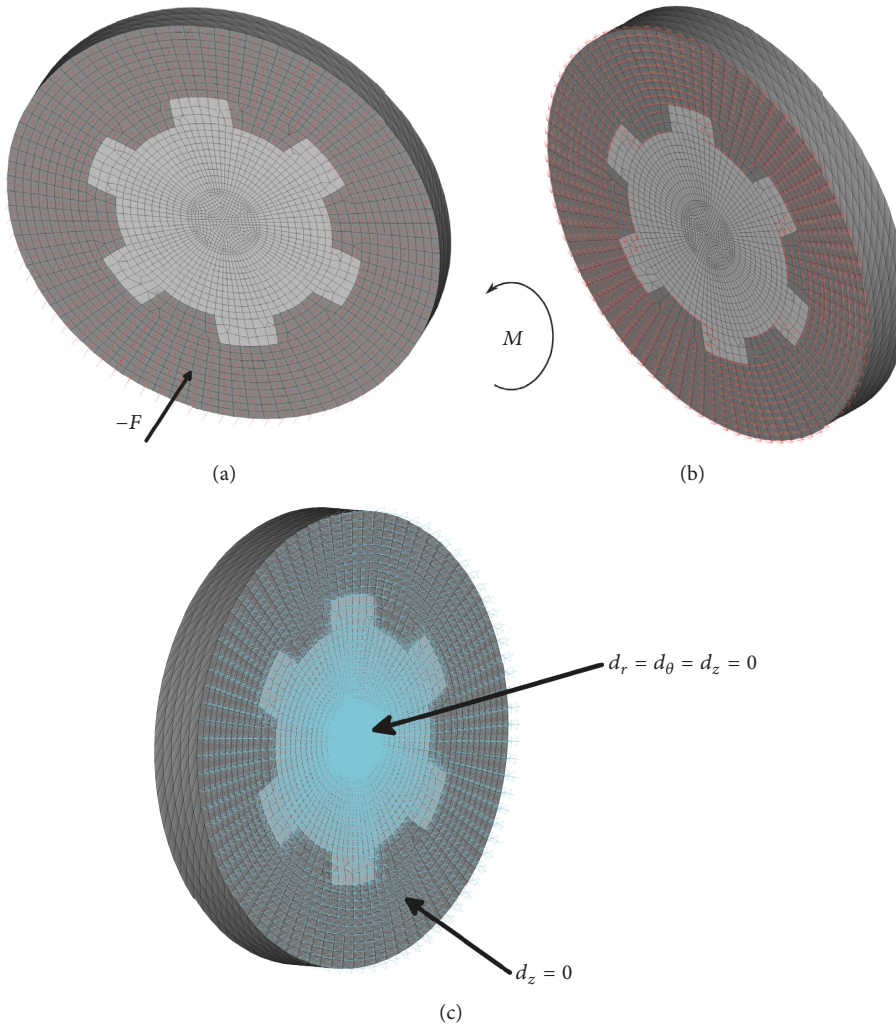


FIGURE 6: Loads and boundary conditions applied to the FEM model of the helical spline coupling ($\beta = 135$ deg): (a) axial force loading (axial section $z = L$), (b) torque loading (axial section $z = L$), and (c) boundary conditions (axial section $z = 0$).

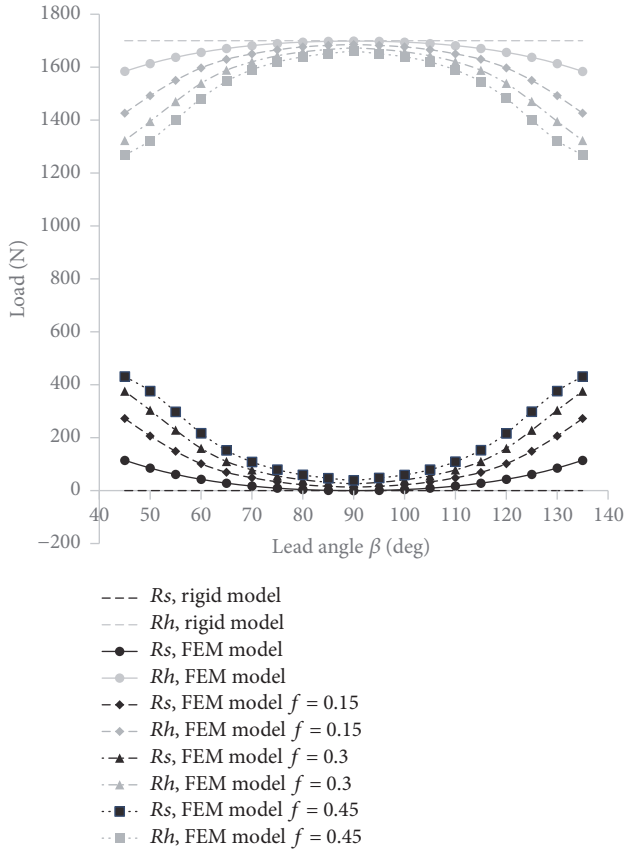


FIGURE 7: Reactions of shaft and hub constraints for different lead angles under axial force load calculated by means of frictionless rigid and FEM model without and with friction.

summing the nodal reactions of the constrained nodes that lie on the corresponding surfaces. Figure 1 enables us to relate the FEM model reactions to the axial thrusts of the device as follows:

$$\begin{aligned} R_h &= F_a \\ R_s &= R. \end{aligned} \quad (3)$$

Accordingly, R_s is the reaction that constraints exert on the grooved part of the shaft and it represents the load transfer R from the hub to the remaining part of the shaft through the spline surfaces. In the same figures, Figures 7 and 8, the corresponding results for a frictionless rigid model are added for the sake of comparison.

The analytical expression of R_s for the frictionless rigid model has been already defined in [12], where it has been found that deformations exert little effects on load transfer in frictionless spline couplings. Indeed, in Figures 7 and 8, the rigid model trends of R_h and R_s (dashed lines) fit the frictionless FEM model corresponding points (circle markers) with low and negligible relative errors, in the order of 1% and 0.1% of the applied axial force and transmitted load, respectively. On the contrary, when a friction factor $f = 0.3$ is assumed, these relative errors (difference between results of frictionless rigid and FEM models with $f = 0.3$) for axial

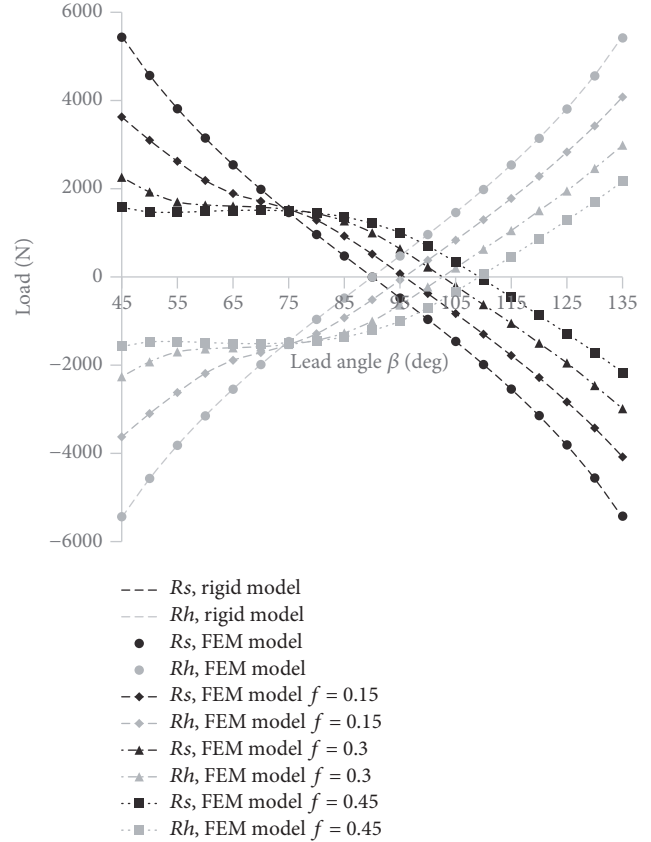


FIGURE 8: Reactions of shaft and hub constraints for different lead angles under torque load calculated by means of frictionless rigid and FEM model without and with friction.

force and torque load cases reach a maximum of 15% for $\beta = 45$ or 135 deg and 140% at $\beta = 45$ deg, respectively. Therefore, the influence of friction on the load transfer is very significant so that the manageable analytical rigid model can be only used as a first approximation in the machine design.

With respect to the straight-tooth spline geometry ($\beta = 90$ deg) for the axial force load case, R_h and R_s curves are symmetric, while for the torque load case they are antisymmetric only when friction is neglected. Particularly, the load transfer R due to torque is not zero for the straight-tooth spline when friction is taken into account. Indeed, since under torque load the rotations of the axial sections increase with their distance from the constrained section, the deformed shape of the straight generatrix of a tooth becomes similar to a helix, as shown in Figure 9, so that the resulting tangential stresses due to friction yield an axial load component.

For both axial force and torque load cases, maximum equivalent stress and maximum contact pressure in the coupling model are plotted as a function of lead angle in Figures 10 and 11, respectively. In comparison with the axial force, the torque load case yields much higher stresses (2 orders of magnitude), as in this condition the coupling behaves like an actuator that without the constraints would cause a relative motion between the shaft and the hub. Therefore, stress due

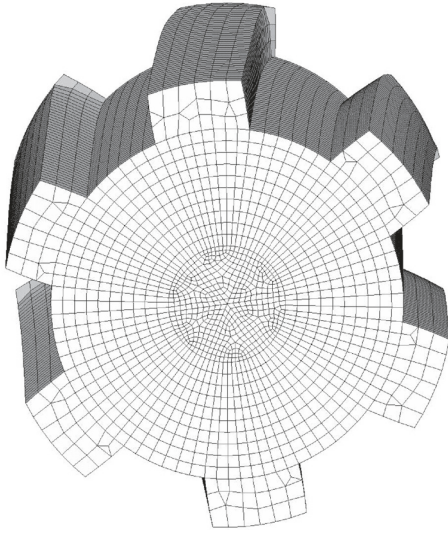


FIGURE 9: Deformed shape of the straight-teeth spline shaft (lead angle $\beta = 90$ deg) under torque local case (magnification factor = 800).

to torque load can exceed yield stress of the material and its effect must be considered in structural design.

For the force load case, maximum equivalent stress and maximum contact pressure trends (Figures 10 and 11) are symmetric with respect to $\beta = 90$ deg. At the same angle, they reach minimum values, since the load transfer $R = R_s$ (Figure 7) is either zero for the frictionless model or very little when friction is considered. Maximum Von Mises stress variations (Figure 10) with helix angle are greater when the lead angle β is lower than 70 deg or higher than 110 deg and the curves tend to become roughly linear. Accordingly, the maximum contact pressures (Figure 11) are higher when helix angles α are greater in magnitude, in agreement with the load transfer rise (Figure 7). Indeed, an increase of R causes contact pressure and, consequently, equivalent stress to grow.

As far as the effect of friction in the force load case is concerned, Figure 7 shows that a growth of the friction factor f tends to level off the hub and shaft reactions (R_h and R_s) by increasing the load transfer R in agreement with equations (2) and (3). Nevertheless, such increase of R due to the rise of f does not yield an increase of maximum stress. On the contrary, it decreases the maximum equivalent stress (Figure 10), since part of the load transfer is carried out by the friction forces, whose magnitude and direction are still unable to cause deformation of the pair members. Such phenomenon can also be observed in Figure 11, where, in comparison with the frictionless model results, limited increases of f cause the maximum contact pressure to drop. Nevertheless, for high values of the friction factor ($f > 0.3$), especially for high magnitude of the helix angle α , maximum contact pressure rises with f due to the action of the high friction forces, which globally increase the deformations. Such trend is also visible in the maximum equivalent stress plot (Figure 10, same values at $\beta = 45$ or 135 deg for $f = 0.3$ and 0.45), although it is less evident and requires higher

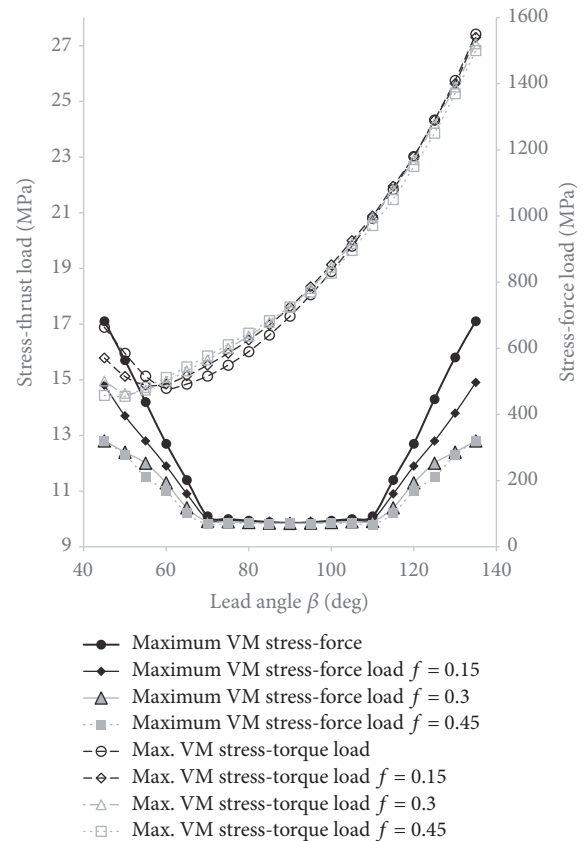


FIGURE 10: Maximum Von Mises stress for different lead angles under axial force load (left ordinate) and torque load (right ordinate) calculated by means of FEM model without and with friction.

values of α and f . Therefore, for a fixed helix angle, the curve of maximum contact pressure as a function of friction factor has a minimum, as shown in Figure 12 for $\beta = 45$ deg. The rise of the contact pressure at high friction factors consequently reduces the variation of maximum equivalent stress (Figure 12).

In the torque load case, maximum equivalent stress and maximum contact pressure trends are not symmetric with respect to the straight-tooth spline configuration (Figures 10 and 11). Indeed, stress and contact pressure intensity depend on the handedness of the spline helix with reference to the torque direction. Similarly, in [15], the numerical simulations of helical gears mounted on shafts by means of helical spline couplings have proved that the selection of a helical spline with the same helix direction as that of the helical gear yields a reduction of the load concentration. Due to such asymmetry, the minima of peak equivalent stress for the frictionless model are reached for $\beta = 60$ deg or lower angles when the friction factor is high (Figure 10).

The friction in the torque load case reduces hub and shaft thrusts as well as the load transfer R (Figure 8) except for the lead angles in the middle of the considered range where R rises with f . Accordingly, maximum contact pressure (Figure 11) decreases by increasing f except for the above-cited β middle range. Maximum Von Mises stress curves

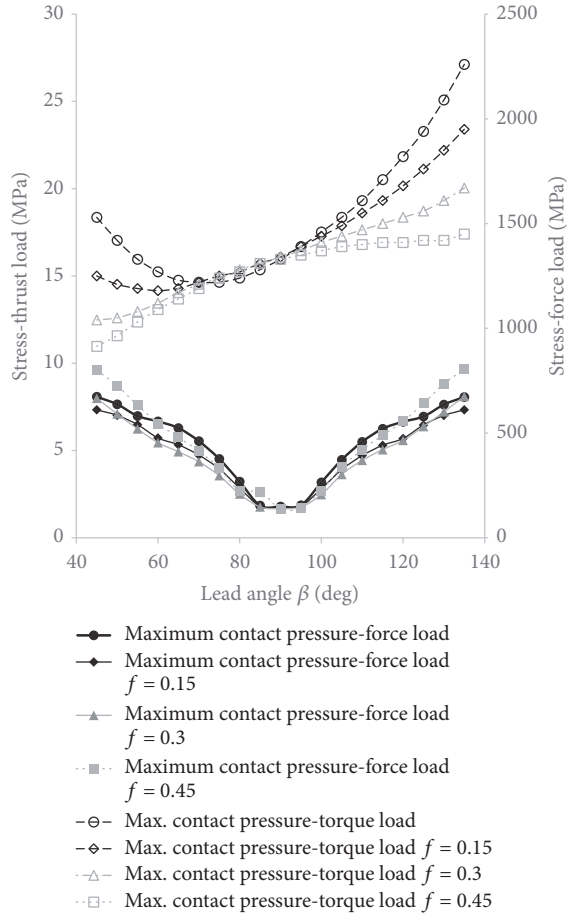


FIGURE 11: Maximum contact pressure for different lead angles under axial force load (left ordinate) and torque load (right ordinate) calculated by means of FEM model without and with friction.

(Figure 10) follow a similar trend to maximum contact pressure plots, although they are less sensitive to friction. The middle region of lead angles where stress increases with f is wider and more shifted to low angles.

Figure 13 depicts the reactions R_h and R_s calculated at the different lead angles under combined load case (simultaneous application of force and torque). Such figure compares the trends obtained by taking advantage of the frictionless rigid model (dashed curves), FEM model with friction ($f = 0.3$, data marked with triangles), and the superimposition of effects (square labels), that is, the sum of the values obtained for $f = 0.3$ by means of the FEM model in two separate analyses, under force and torque loads. The plot confirms that friction and deformations must be taken into account and the superimposition of effects is not valid due to the non-linear behavior of the model. The corresponding maximum equivalent stress and maximum contact pressure trends are plotted in Figure 14. As far as such parameters are concerned, in comparison with reaction curves, superimposition of effect yields better agreement with the FEM model results obtained under combined load. For the sake of structural strength, the design lead angle should be as low as possible. Particularly,

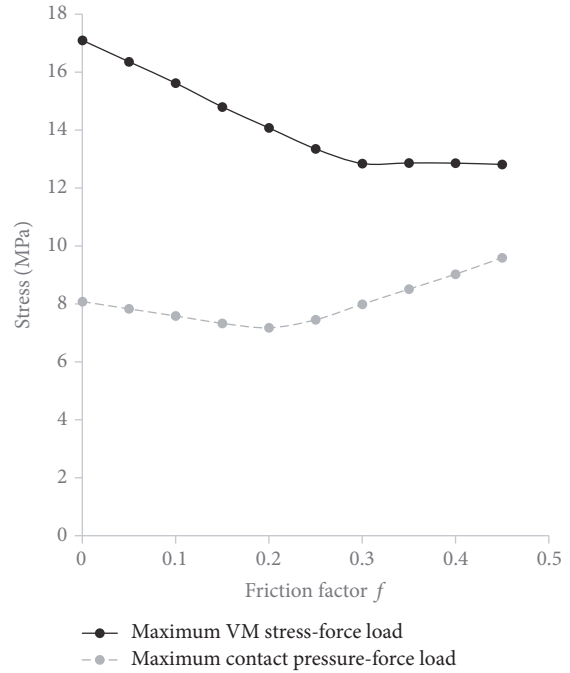


FIGURE 12: Maximum Von Mises stress and maximum contact pressure for different friction factors at a constant lead angle ($\beta = 45$ deg) under axial force load calculated by means of FEM model.

maximum Von Mises stress exceeds 1000 MPa for lead angles greater than 110 deg.

6. Design of the Support System

A simple method to choose the helix angle has been previously published in [12], where it is only applied to load case B, and the effects of friction, axial force, and deformations of the helical spline coupling (6) are neglected. In the present paper, all of these effects are taken into account in order to improve the design method.

The relevant graphical construction, shown in Figures 15 and 16, is aimed at finding the possible design range for the lead angle β . To this end, the load transfer R through the coupling together with the corresponding axial loads F_a and F_s of the bearings (4) and (3), respectively, is plotted as a function of the lead angle β in nominal working conditions. In Figures 15 and 16, the constant trends (thick solid lines), which plot the magnitude of the resultant load T_{ref} , can be compared with F_a in order to assess for which lead angles the main thrust bearing is either penalized or favored in comparison with a conventional support system [12]. The trends R are computed by means of either the FEM model for a friction factor $f = 0.3$ and combined load case or the frictionless rigid model. The corresponding curves of F_a and F_s are found by means of equation (2). In case B (Figure 15), the curves of the load transfer R for frictionless rigid and FEM model ($f = 0.3$) are the same as plotted in Figure 13, where both torque ($M = M_t$) and compressive axial force ($F = T_t < 0$) are considered in the numerical analysis. Differently, in case A (Figure 16), a new plot of R is calculated

TABLE 3: Design ranges of lead angles in the two load cases calculated by means of the different models.

Load case	Model	β_{\min} [deg]	β_{\max} [deg]
B	Frictionless rigid	72.0	77.4
B	FEM $f = 0.3$	81.0	88.2
A	Frictionless rigid	95.4	100.8
A	FEM $f = 0.3$	108.9	115.2

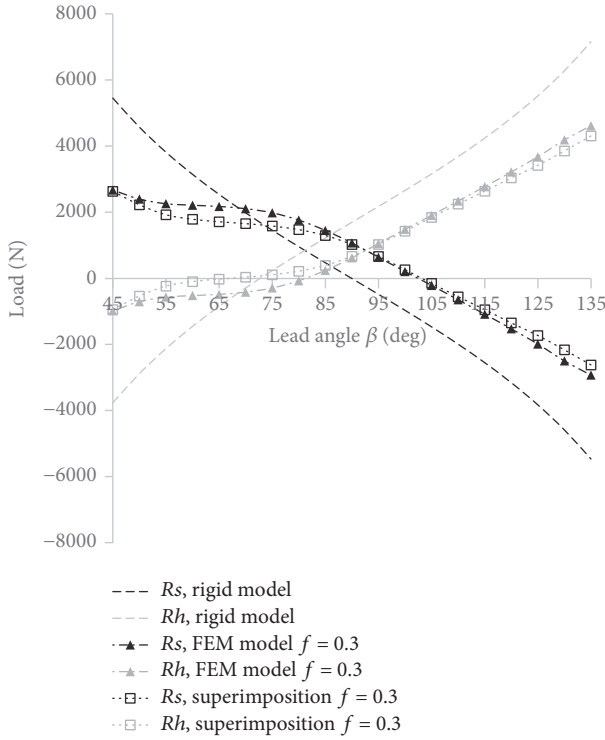


FIGURE 13: Reactions of shaft and hub constraints for different lead angles under combined load calculated by means of the frictionless rigid and the FEM model (friction factor = 0.3) as well as by summing results from analyses under force and torque loads.

by simultaneously applying torque and tensile axial force ($F = T_t > 0$) to the FEM model ($f = 0.3$). Such calculation is compulsory, as the coupling model is nonlinear.

For the reasons explained in [12], the method of locating the limits for the possible design values of β consists in finding the zeros of the functions $F_a = F_a(\beta)$ and $F_s = F_s(\beta)$. Such zeros enclose the design range of the lead angles and they are represented by star symbols in Figures 15 and 16, where white and gray stars are related to FEM and rigid model, respectively. The corresponding design limits of the lead angle β for load cases A and B are summarized in Table 3. Such table evidences that the helix angles admissible for design purpose roughly span either 5 deg (rigid model) or 6 deg (FEM model), and friction and deformation tend to increase the angles that mark the boundaries of the design range.

As explained in the case study paragraph, for different impeller geometries, nominal compressor, turbine, and total

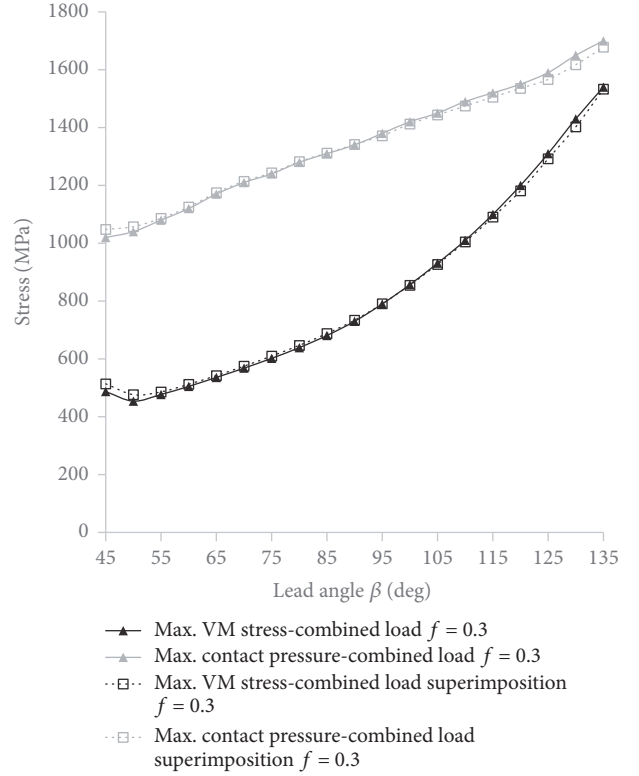


FIGURE 14: Maximum equivalent stress and contact pressure for different lead angles under combined load calculated by means of the FEM model (friction factor = 0.3) as well as by summing results from analyses under force and torque loads.

thrust can vary noticeably in intensity and reverse. Therefore, the range of design helix angles may considerably change with the impeller design. As a rule, the design limits of β must be included within the range of lead angles feasible for helical spline couplings and gears; that is, β must be in the range of 45–90 deg when both compressor and turbine thrusts are directed toward the inner side of the machine and the resultant thrust is negative, as in case B.

Differently, when the resultant thrust is positive ($T_{\text{ref}} > 0$, as in case A), according to the proposed graphical construction, the trend of the load transfer R must reach negative values in order to make the thrust functions (F_a and F_s) zero, as shown in Figure 16 and suggested by equation (2). According to load transfer results, this is possible if the lead angle β is greater than 90 deg, that is, by means of a reversal of the helix handedness. Again, the lead angle cannot exceed 135 deg, which is a safe operation limit for the actuator, like in helical gears.

In a nutshell, with reference to Figure 2, if the total thrust load in nominal conditions is negative ($T_{\text{ref}} < 0$, as in case B), the active bearing is located on the right side of the runner and the lead angle β of the spline coupling (6) is lower than 90 deg. Conversely, if the resultant nominal thrust is positive ($T_{\text{ref}} > 0$, as in case A), the active bearing is on the left side of the runner and $\beta > 90$ deg.

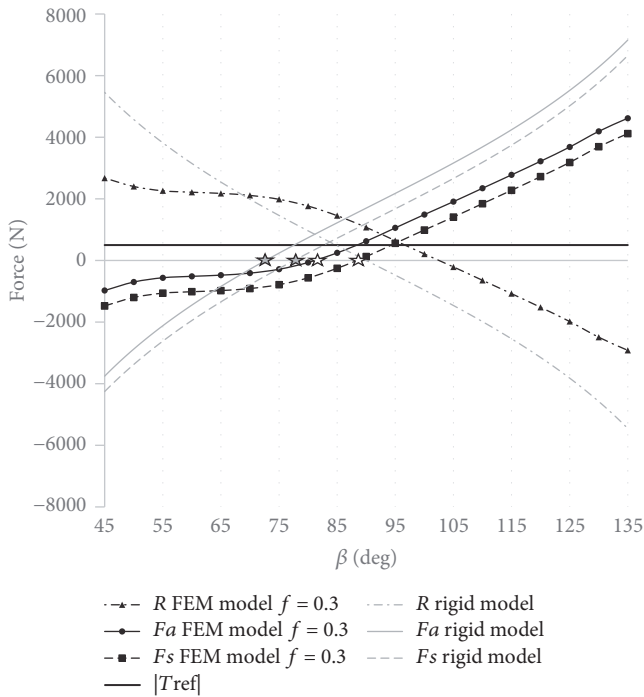


FIGURE 15: Graphical design method: trends of axial bearing thrusts and load transfer as a function of lead angle in nominal operating conditions in case B.

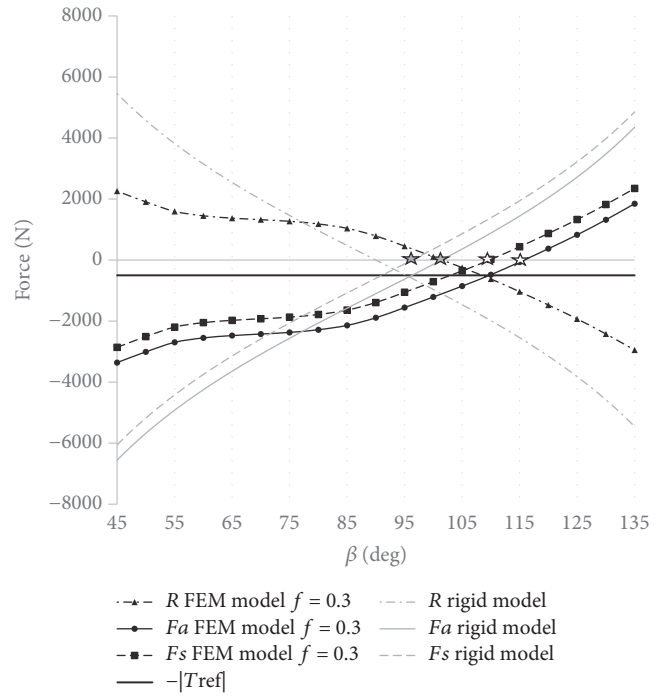


FIGURE 16: Graphical design method: trends of axial bearing thrusts and load transfer as a function of lead angle in nominal operating conditions in case A.

In wider terms, the helix angle of the spline coupling (6) can be chosen with reference to the nominal working conditions on the basis of the target life of the bearings within a suitable range, whose limits are assessed by means of the proposed graphical construction. The resulting choice of lead angle β must finally fall within the admissible range of 45–135 deg.

7. Conclusions

The conceptual design of an innovative support system capable of drastically improving start/stop performance of modern oil-free micro-GT has been concluded. The rolling-element bearings used in the paper in order to explain the device may be substituted with oil-free magnetic bearings so that a support system with lower current consumption in comparison with systems totally based on AMBs is obtained. The invention can also be used to retrofit the older machines, whose shaft is mounted on rolling-element bearings. Such retrofit cannot be done by means of conventional support systems based on foil air bearings [8].

In order to perform the detailed design of the invention, structural FEM analyses of the helical spline employed as load partition as well as coupling device have been carried out. Numerical calculations have shown that

- (i) load partition of the spline coupling strongly depends on friction, which cannot be neglected in the detailed design of the device;
- (ii) axial load and deformation of the coupling are also influent on load partition; they can only be neglected as first approximation;

- (iii) deformation and friction tend to level off the thrusts transmitted by the shaft and the hub;
- (iv) the handedness of the helical spline coupling with respect to the applied torque direction is influential on stress and contact pressure magnitude.

Finally, the previously presented method for the helical spline design [12] has been refined in order to take into account of the above-cited findings. It has been also adapted to the double-effect thrust air bearings, showing that the handedness of the helical spline must be chosen on the basis of which bearing is active in nominal working conditions.

Such graphical method has been applied by taking advantage of the new numerical results. The results show that friction and deformation increase the design helix angles.

In the future, a detailed design of the invention will be further studied by considering involute spline profiles as well as by calculating the optimal hot clearances of both thrust bearings and turbine hub-shaft coupling by means of elastoaerodynamic analysis of the thrust foil bearing lubrication.

Nomenclature

- B : Spline side distance, mm
- c : Clearance, μm
- d : Displacement, mm
- D : Diameter, mm
- f : Friction factor
- F : Axial load, N

L :	Spline coupling length, m
M :	Torque, Nm
n :	Number of splines
N :	Rotational speed, rpm
P :	Power, kW
r :	Radius, mm
R :	Reaction, N
T :	Thrust, N
x, y, z :	Spline coupling Cartesian coordinate system
W :	Bearing radial load, N
α :	Helix angle, deg
β :	Lead angle, deg.

Subscripts

c :	Compressor
h :	Hub
o :	Outer
p :	Pitch
r :	Radial direction
s :	Shaft
t :	Turbine
ref:	Reference
z :	Axial direction
ϑ :	Circumferential direction.

Data Availability

All of the data obtained from this study are contained within the present manuscript and [12].

Conflicts of Interest

The authors declare that there are no conflicts of interest regarding the publication of this article.

Acknowledgments

The authors would like to thank their patent consultant Dr. Andrea Grimaldo for the useful discussion of the results published in the present paper during the preparation of the documentation of the national patent and PCT.

References

- [1] D. J. Clark, M. J. Jansen, and G. T. Montague, *An Overview of Magnetic Bearing Technology for Gas Turbine Engines*, NASA-TM—2004-213177, 2004.
- [2] R. Moser, J. Sandtner, and H. Bleuler, "Optimization of repulsive passive magnetic bearings," *IEEE Transactions on Magnetics*, vol. 42, no. 8, pp. 2038–2042, 2006.
- [3] J. Hillyard, "Magnetic bearings," in *Proceedings of the Joint Advanced Student School Conference (JASS '06)*, pp. 1–15, St. Petersburg, Russia, April 2006.
- [4] A. Irving and J. Ibets, "High-Speed Bearing Technologies for Wastewater Treatment Applications," in *Proceedings of the Water Environment Federation (WEFTEC '13)*, vol. 2013, pp. 98–106.
- [5] B. J. Hamrock and W. J. Anderson, *Rolling-Element Bearings*, NASA RP-1105 1–58, 1983.
- [6] C. Dellacorte, V. Lukaszewicz, M. J. Valco, K. C. Radil, and H. Heshmat, "Performance and durability of high temperature foil air bearings for oil-free turbomachinery," *Tribology Transactions*, vol. 43, no. 4, pp. 774–780, 2000.
- [7] G. L. Agrawal, "Foil air/gas bearing technology - An overview," in *Proceedings of the ASME 1997 International Gas Turbine and Aeroengine Congress and Exhibition (GT '97)*, USA, June 1997.
- [8] K. C. Radil and C. Dellacorte, *Foil Bearing Starting Considerations and Requirements for Rotorcraft Engine Applications*, 2009.
- [9] C. E. Fanning and T. A. Blanchet, "High-temperature evaluation of solid lubricant coatings in a foil thrust bearing," *Wear*, vol. 265, no. 7-8, pp. 1076–1086, 2008.
- [10] H. Heshmat, P. Hryniewicz, J. F. Walton II, J. P. Willis, S. Jahanmir, and C. DellaCorte, "Low-friction wear-resistant coatings for high-temperature foil bearings," *Tribology International*, vol. 38, no. 11-12, pp. 1059–1075, 2005.
- [11] Y. Masato, *Foil Bearing*, 2015.
- [12] F. Stefani, A. Perrone, L. Ratto, and R. Francesconi, "Comparative analysis of bearings for micro-GT: an innovative arrangement," in *Bearing Technology*, P. H. Darji, Ed., pp. 1–26, InTech, Rijeka, Croatia, 2017.
- [13] J. R. Mancuso and R. Jones, "Coupling interface connection," in *Proceedings of the 30th Turbomachinery Symposium*, pp. 121–138, Texas A & M University, 2001.
- [14] M. Balasubramaniam, E. Golaski, S.-K. Son, K. Sriram, and A. Slocum, "An anti-backlash two-part shaft coupling with interlocking elastically averaged teeth," *Precision Engineering*, vol. 26, no. 3, pp. 314–330, 2002.
- [15] J. Hong, D. Talbot, and A. Kahraman, "Load distribution analysis of clearance-fit spline joints using finite elements," *Mechanism and Machine Theory*, vol. 74, pp. 42–57, 2014.
- [16] D. Barsi, T. Garbarino, A. Perrone et al., "Micro gas turbine integrated design: thermodynamic cycle, combustor, recuperator and bearings (Part 1)," in *Proceedings of the The 4th International Conference on Water Resource and Environment (WRE '15)*, 2015.
- [17] A. M. Davis, *Thrust Balancing*, 1956.

